Research Article

Perfluorocarbon/Gold Loading for Noninvasive in Vivo Assessment of Bone Fillers Using 19F Magnetic Resonance Imaging and Computed Tomography

Simone Mastrogiacomo,[†] Weiqiang Dou,[‡] Olga Koshkina,[§] Otto C. Boerman,[‡] John A. Jansen,[†] Arend Heerschap,[‡] Mangala Srinivas,[§] and X. Frank Walboomers*,[†]

[†]Department of Biomaterials, Radboud University Medical Center, P.O. Box 9101, 6500 HB Nijmegen (309), The Netherlands

[‡]Department of Radiology and Nuclear Medicine, Radboud University Medical Center, Geert Grooteplein Zuid 10, 6525 GA Nijmegen, The Netherlands

[§]Department of Tumor Immunology, Radboud Institute for Molecular Life Sciences (RIMLS), Geert Grooteplein Zuid 28, 6525 GA Nijmegen, The Netherlands

S Supporting Information

ABSTRACT: Calcium phosphate cement (CPC) is used in bone repair because of its biocompatibility. However, high similarity between CPC and the natural osseous phase results in poor image contrast in most of the available in vivo imaging techniques such as computed tomography (CT) and magnetic resonance imaging (MRI). For accurate identification and localization during and after implantation in vivo, a composition with enhanced image contrast is needed. In this study, we labeled CPC with perfluoro-15-crown-5-ether-loaded (PFCE) poly-(latic-co-glycolic acid) nanoparticles (hydrodynamic radius 100 nm) and gold nanoparticles (diameter 40 nm), as 19F MRI and CT contrast agents, respectively. The resulting CPC/PFCE/gold composite is implanted in a rat model for in vivo longitudinal imaging. Our findings show that the incorporation of the two types of different nanoparticles did result in adequate handling properties of the cement. Qualitative and quantitative long-term assessment of CPC/PFCE/gold degradation was achieved in vivo and correlated to the new bone formation. Finally, no adverse biological effects on the bone tissue are observed via histology. In conclusion, an easy and efficient strategy for following CPC implantation and degradation in vivo is developed. As all materials used are biocompatible, this CPC/PFCE/gold composite is clinically applicable.

Perfluorocarbon-loaded PLGA nanoparticle

Gold nanoparticle

19F-MRI and CT dual-labeled bone substitute
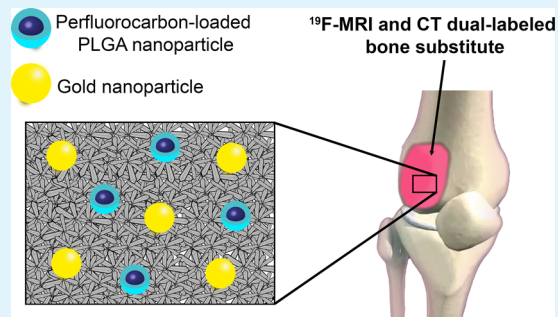
1. INTRODUCTION

Bone grafting is the most common transplantation procedure, after blood, with more than 2 million patients worldwide receiving a bone transplant every year.[1,2] To date, autografting of autologous bone is still the *gold standard* procedure. However, drawbacks such as the need for a second surgery, high donor-site morbidity, and shortage of donor bone are increasing the demand for artificial bone substitutes. Since 1920, calcium phosphate-based cement (CPC) has been extensively studied and used for orthopedic and dental applications due to its high biocompatibility, biodegradability, and osteoconductivity.[3−5] Moreover, the ability to be injected and to set at body temperature in vivo makes CPC suitable for minimally invasive surgeries.[6] Two criteria are important in the application of CPC in bone repair: mechanical properties that are tailored to the specific application and an adequate imaging contrast that allows for monitoring cement after injection, particularly to monitor its degradation.[6,7] However, only a few

strategies have been successful in the synthesis of CPC that meet both criteria, as labeling the cement typically affects its mechanical properties. X-ray and CT are the most common methods to monitor bone defects and the formation of new bone.[8,9] Nonlabeled CPCs have a slightly higher radiodensity than the natural bone, resulting in a brighter signal on conventional X-ray radiographs. However, the geometrical conformation of the cement is barely recognizable after surgery. Longitudinal monitoring becomes even more challenging when degradation of the material and the in-growth of the new bone begins.[10−12] Addition of radiopaque salts, such as barium sulfate or tantalum oxide, can enhance the radiocontrast of CPC without affecting its biological behavior.[13−16] However, the incorporation of such salts affects the setting and mechanical

properties of the cement, making it less suitable for clinical application. To avoid changes in cement properties after labeling, different strategies, such as the encapsulation of probes into a silica carrier, have been described.[17,18] Also, gold nanoparticles (AuNPs) are promising for CT because gold has a high atomic number (Z = 79) and high X-ray attenuation per mass (5.16 cm^2 g^{-1} at 100 keV). Moreover, biocompatibility, low toxicity, and high affinity of gold nanoparticles to different functional groups, for example thiol or phosphine, make AuNPs suitable for labeling biomaterials.[19−21] However, no successful strategy for long-term labeling of CPC with gold has been described thus far.

MR imaging of hard tissues (i.e., bone and teeth) requires acquisition sequences sensitive to their very short transversal relaxation such as ultrashort echo time (UTE) and zero echo time (ZTE) sequences.[22,23] However, in MR images with these sequences, bone transplants do not provide enough contrast, making labeling essential.[24] Multimodal imaging with MRI and CT is advantageous, as it allows the acquisition of independent information using two different imaging techniques. The use of two independent labels with different physicochemical properties and different affinity to CPC could reduce problems such as a decrease or complete loss of the signal due to, for example, diffusion of noncovalently attached label from the CPC matrix. The first CPC mixture that was labeled with multiple imaging agents contained superparamagnetic iron oxide particles (SPIO, 200 nm in diameter) and colloidal gold (4 nm in diameter) respectively as MRI and CT contrast agents.[17,18] However, the strong susceptibility artifacts caused by SPIO particles resulted in a gross overestimation of the implant shape.[25,26] Together with the fast decrease of the CT contrast over time, the use of this strategy became very limited. The labeling of CPC with heteronuclei, such as ^{19}F, ^{31}P, or ^{23}Na, natural isotopes with spin of 1/2 that can be directly detected with MRI, could be an excellent alternative to SPIO. Fluorine is especially attractive as it is almost completely absent from biological tissues, which results in a high MR contrast-to-noise ratio and specificity, and it has a similar intrinsic high sensitivity as that of protons.[27−32] Typical ^{19}F MRI labels contain organofluorine compounds, in particular liquid perfluorocarbons (PFCs). Perfluorocarbons are biologically inert and exhibit low toxicity. Therefore, they have been used in the clinic as blood substitutes and more recently as MR imaging agents.[33−36]

In this study, we combined ^{19}F MRI and CT for imaging the CPC in bone for the first time, using perfluoro-15-crown-5-ether (PFCE)-loaded poly(D,L-lactide-co-glycolide) (PLGA) nanoparticles and commercially available gold nanoparticles (AuNPs). PFCE nanoparticles have previously only been applied to image labeled cells, i.e., soft tissues.[35] Here we use these nanoparticles for imaging of bone substitutes. We decided to use AuNPs because they are also effective for both promoting osteoblast differentiation and bone formation.[37,38] This newly developed CPC/PFCE/gold composite was first characterized in vitro and then implanted in vivo in a rat femoral condyle model. We followed material degradation by in vivo ^{1}H/^{19}F MRI and CT up to 8 weeks postsurgery and correlated the images to the biological tissue response.

2. MATERIALS AND METHODS

2.1. CPC Composite.
Calcium phosphate cement (CPC) was prepared as a w/w mixture of 78.5% α-tricalcium phosphate (α-TCP; CAM Bioceramics BV, Leiden, The Netherlands), 1.5% carboxymethylcellulose (CMC; CAM Bioceramics), and 20% of cryo-grinded poly(D,L-lactide-co-glycolide) microparticles (<200 μm) with a 50:50 ratio of lactic to glycolic acid (PURASOB 5002A, Purac, Gorinchem, The Netherlands).

2.2. Contrast Agents.
PFCE-loaded PLGA nanoparticles were prepared as described elsewhere.[35] Briefly, PLGA (100 mg) was dissolved in dichloromethane (3 mL) and mixed with PFCE (0.9 mL) and Prohance (1.78 mL). The resulting emulsion was added quickly under sonication to 25 mL of 1.96% (w/w) solution of poly(vinyl alcohol) (9−10 kDa, 80% hydrolyzed) and sonicated for 3 min at 40% amplitude (Branson Digital Sonifier 250; Branson Sonic power, Danbury, CT). After evaporation of the solvent overnight the particles were washed four times with water at 16 000g, resuspended in water, and freeze-dried, yielding of approximately 100−150 mg of particles as white powder. PFCE was purchased from Exfluor, Rond Rock, TX; PLGA Resomer RG 502H, lactide:glycolide molar ratio 48:52−52:48, from Evonic, Germany; dichloromethane from Merck, Darmstadt, Germany; and PVA from Sigma-Aldrich, St. Louis, MO.

Gold nanoparticles (diameter 40 nm) stabilized by citrate in 0.1 mM phosphate buffered saline solution (PBS) were purchased from Sigma and used without any additional modification.

2.3. Material Preparation.
The CPC control (i.e., without contrast agents) was prepared by adding the mixed powders (i.e., α-TCP, CMC, and PLGA) into an exit-closed 2 mL syringe (Terumo Europe N.V., Leuven, Belgium). Afterward, 50 μL of sterile-filtered (0.2 μm filter) sodium dihydrogen phosphate solution (4% NaH$_2$PO$_4$· 2H$_2$O) was added into the syringe and shaken for 30 s by means of a dental shaker machine (Silamat mixing apparatus, Vivadent, Schaan, Liechtenstein).

In order to add the contrast agents to the starting CPC composition, additional steps were requested. Briefly, 100 mg of initial powders of CPC was first mixed with 1 mL of AuNPs solution (corresponding to ~7.2 × 10^9 particles), homogenized by vortex, and freeze-dried overnight. Thereafter, 20 mg of PLGA/PFCE nanoparticles was first resuspended in 1 mL of Milli-Q water and then added to the CPC/gold powder. The solution was then vortexed and freeze-dried again providing the final composition, which is indicated in this study as CPC/PFCE/gold.

An additional CPC composite was prepared by performing the same freeze-dry steps as described before, but using Milli-Q water alone, without any contrast agents. This CPC/freeze-dry composite was used as an internal control for the characterization of the handling and mechanical properties. Samples were sterilized by using 25 kGy of γ radiation (Synergy Health Ede B.V., Ede, The Netherlands).

2.4. Material Characterization.
Morphological assessment of the PFCE-loaded PLGA nanoparticles and of preset cylinders of CPC/PFCE/gold were performed by electron scanning microscopy (SEM, JEOL 6310, Jeol Corp., Tokyo, Japan). Images were acquired at 5 kV with ×5000 magnification.

The size and the zeta potential of the PLGA/PFCE nanoparticles were measured by dynamic light scattering (DLS) using a Malvern Zetaziser Nano ZS (Malvern Instrument, Worcestershire, UK) at sample concentration of 0.1 mg/mL, using ultrapure water as a solvent for DLS and 5 mM sodium chloride solution for zeta potential measurements. The content of PFCE was determined by ^{19}F NMR (Bruker Avance 400) using trifluoroacetic acid as an internal reference and deuterium oxide as solvent (both from Sigma-Aldrich).

2.5. Cement Handling and Mechanical Properties.
Setting times, elasticity, compression strength, injectability, and cohesion properties of the CPC with and without contrast agents were investigated. As internal control the CPC/freeze-dried composite was also used.

For the setting times, a Gillmore apparatus according to ASTM C266 was used. The cement pastes were injected in a cylindrical bronze mold of 6 mm in diameter and 12 mm in height and immersed in a water bath at 37 °C after which initial and final setting times were recorded. The elasticity and the compressive strength were calculated by using a testing bench machine (858 miniBionixII, MTS, Eden Prairie, MN). Cylinders of 4.5 mm in diameter and 9 mm in height were prepared from the CPC mixtures and compressed with a loading force of 2.5 kN at a constant speed of 0.5 mm min^{-1}. The injectability

was assessed by using the same testing bench machine (858 miniBionixII) set in a compression mode and adapted with a custom-made fixture metallic cage. A total weight of 500 mg for each cement composition was mixed into an exit-closed 2 mL syringe (Terumo Europe N.V.) with 250 μL of setting solution (4% $NaH_2PO_4\cdot2H_2O$). After mixing the components for 30 s, the syringe was placed in the metallic cage, the exit was opened, and a compression force of 100 N (i.e., estimated maximum force applicable by human operator) was applied with a constant speed of 20 mm min^{-1} until all the material was extruded from the syringe (33 ± 2 s). From the raw data the extrusion curve was obtained as reported in the literature as applied force (N) by the time (s).[39] Finally, all the cements extruded from the syringes were accumulated in 10 mL of PBS at 37 °C, and the cohesive properties were qualitatively assessed (i.e., by counting the number of fragments).

2.6. In Vitro Assay. A cylindrical hole (3 × 3 mm) was drilled into bone blocks (~1 cm^3) obtained from pig cadaver jaw. The hole was filled either with CPC or CPC with contrast agents and cured overnight. All the samples were prepared in triplicate (n = 3).

For MRI scan, the samples were first embedded in 5% gelatin type A (Sigma-Aldrich) in order to simulate a water environment. The gelatin was poured in a 15 mL plastic tube and solidified at +4 °C. For the microcomputed tomography (μCT) measurements the samples were wrapped in Parafilm (SERVA Electrophoresis GmbH, Heidelberg, Germany) to avoid drying artifacts during the scan.

2.7. In Vitro μCT. The bone blocks were scanned horizontally along the X-ray beam by using a μCT imaging system (Skyscan 1072, Kontich, Belgium). Samples were recorded using ×15 magnification (i.e., pixel resolution = 18.88 μm), X-ray source of 100 kV/98 μA, exposure time 3.9 s, and 1 mm aluminum filter. The obtained projected files were reconstructed with NRecon software (Skyscan) and analyzed with CtAnalyser software (version 1.10.1.0; Skyscan). The volume of interest (VOI) was defined manually by selecting a total of 135 slices (in height; i.e., 2.55 mm) and a circle of 3 mm (in diameter). Two-dimensional (2D) reconstructions were finally obtained by DataViewer software (Version 1.5.2.4; Skyscan).

2.8. In Vitro MRI. All the samples embedded in gelatin were scanned on a 11.7 T MRI system (Biospec, Bruker, Germany) equipped with a ^{1}H/^{19}F volume coil. ^{1}H/^{19}F MR images of the bone phantom were acquired by a zero echo time (ZTE) sequence with the following parameters: repetition time (TR) = 2 ms/4 ms, image resolution = 1.56 × 1.56 × 1.56 mm, 1 average/16 averages, flip angle (FA) = 2°/4°, and acquisition time (TA) = 27 s/13.54 min. The obtained ^{1}H and ^{19}F MR images were processed with Matlab R2014b (MathWorks Inc., Natick, MA) and overlaid by using MRIcro software (Smith Micro software, Aliso Vijeo, CA).[40]

2.9. In Vivo Assay. The animal study was performed in agreement with the standards and the protocols of the Radboud University Medical Center, Nijmegen, The Netherlands. All the surgeries were performed after the approval of the Animal Ethics Committee (RU-DEC number 2015-0035) for the care and the use of laboratory animals. Sixteen healthy male Wistar rats (body weight: 250−300 g) were used as experimental animals. A rat femoral condyle defect model was used as described elsewhere.[42] In order to reduce the number of animals for this experiment, both posterior legs of the animals were used. First, the animal was anesthetized by inhalation of a mix of Isoflurane (Rhodia Organique Fine, Avonmouth, Bristol, UK) and oxygen, and then the legs were shaved and disinfected using povidone−iodine solution. The animal was located in the supine position on a heating mat in order to prevent hypothermia. A longitudinal incision was performed through the skin and the muscle on the medial surface of the knee (Supporting Information Figure S1). After the exposition of the medial side of the distal femoral condyle, the patella was laterally dislocated in order to have a clear view of the knee joint. Three different dental burs with increasing diameter up to 2.5 mm were used in order to perform a cylindrical defect (2.5 mm in diameter and 3 mm in depth) along the same direction of the femur. A sterile 0.9% saline solution (Fresenius Kabi B.V., Emmer-Compascuum, The Netherlands) was used to cool down the dental bur and to clean the drilled cavity. In the meantime, the CPC powders were

mixed with the setting solution as described before. The defect was filled with CPC with or without contrast agents, while it was left empty in the case of the positive control group. As negative control group, the leg was kept untreated (Table S1). After cement implantation, the patella was moved back to the original position, and the muscle and the skin were closed with absorbable sutures (Vicryl 4.0 Ethicon, Somerville, NY). A subcutaneous injection of pain killer (5 mg/mL Rimadyl, Pfizer animal health, NY) was performed postsurgery in order to decrease postoperative discomfort. After the MRI and CT scans the skin was further fastened by using metallic wound clips (Becton and Dickinson, Franklin Lakes, NJ). In vivo MRI and CT were performed right directly postoperative and at 4 and 8 weeks postsurgery. After 8 weeks the animals were sacrificed by CO_2/O_2 inhalation, and the femora were harvested for histological assessments.

2.10. In Vivo CT. For the in vivo CT a small animal CT scanner was used (Inveon Micro-CT/PET, Siemens Medical Solution, Knoxville, TN). The animals were located in the supine position on a heating mat and always assessed under general anesthesia (Isoflurane/O_2). Images were recorded with an acquisition time of 6 min, spatial resolution of 30 μm, 80 kV tungsten anode source, and exposure time of 1000 ms. Inveon Research Workplace (IRW, Siemens) software was used for 3D reconstruction of the projected files and in order to define the VOI corresponding to the implanted material. As the shape of the implant was heterogeneous from leg to leg, the outline of the implant was carefully drawn. For each VOI, the total volume in mm^3 and the mean attenuation intensity in Hounsfield units (HU) were calculated. For each implant, the level of attenuation intensity was adjusted by the corresponding volume. Finally, the mean value of the signal intensity at each time point was computed. Signal decrease over time was also investigated. Based on a constant VOI (of 15 mm^3), the relative signal intensity at each time point was expressed as percentage and calculated as total signal intensity from the implants to the mean of the signal intensity from normal bone (i.e., no defect group) (Figure S2).

2.11. In Vivo MRI. Animal MR experiments were performed with the same 11.7 T MRI system and ^{1}H/^{19}F volume coil as for in vitro experiments. Animals were anesthetized by Isoflurane/O_2 and placed in the supine position. One by one each leg was immobilized inside the coil while body temperature and breathing were constantly monitored. For fluorine content quantification a 200 mL Eppendorf tube filled with 20 mg of PLGA/PFCE nanoparticles dispersed in Milli-Q water was used as reference. The Eppendorf tube was placed adjacent to the medial side of the leg. ^{1}H/^{19}F images for each rat leg were acquired by ZTE sequence with TR = 2 ms, image resolution = 0.31 mm^3/1.25 mm^3, 1 average/32 averages, and FA = 2°/4°. The scan times were less than 7 and 14 min for ^{1}H and ^{19}F, respectively. The ^{19}F signals in the rat legs as well as in the control sample were quantified in MRIcro software.[40] Regions of interest (ROIs) were manually outlined based on the detected ^{19}F signal on ^{19}F ZTE images. ^{19}F signal per ROI was calculated through multiplying the mean of the pixel intensity of the ROI by its volume (i.e., area per slice thickness). The total ^{19}F amount was then summed over slices and expressed in arbitrary units (au).[41] Based on the quantified ^{19}F signals of the control sample scanned together with each leg at day 0, 4, and 8 weeks, the normalization procedure for ^{19}F signals has also been performed within each leg at three time points and between legs.

2.12. MRI, CT, and Implant Volume Linear Correlation. Correlation analysis was performed by comparing ^{19}F MRI signal (expressed in au), CT signal (expressed in HU/mm^3), and volume of the implant (expressed in mm^3) at each time point. The volume of the implant at each time point was calculated by IRW (Siemens) based on the in vivo CT acquisitions. For each time point, the two-tailed Pearson correlation coefficient (ρ) between MRI signal and volume of the implant, CT signal and volume of the implant, and CT signal and MRI signal was calculated. Afterward, Pearson coefficients were converted to Fisher's coefficient (z), and the interval of confidence at 95% was computed by backconverting z to ρ. Pearson coefficients were ranked according to the rule of thumb.[43]

2.13. Histology. Samples were decalcified in 10% ethylenediaminetetraacetic acid (EDTA) for 2 weeks. The decalcified

bones were then dehydrated in a gradual ethanol series (from 70% to 100%) and embedded in paraffin. Sections of 4 μm in thickness were cut along the axial direction of the femur by using a microtome (RM2165, Leica Microsystems, Rijswijk, The Netherlands). The sections were stained with hematoxylin/eosin (H/E) and with trichrome Elastic van Gieson (EVG). For each specimen, at least two images from three sections (at 100 μm of interdistance) were analyzed. Images were acquired by using a light microscope (Axio Imager Z1, Carl Zeiss AG Light Microscopy, Göttingen, Germany) equipped with a digital camera (AxioCam MRc5, Carl Zeiss AG Light Microscopy). Histomorphometrical analysis was performed based on the EVG-stained slices by using a computer image analysis technique based on ImageJ software (Wayne Rasband, Research Services Branch, National Institute of Mental Health, Bethesda, MD). The amount of bone was calculated as area percentage inside a defined ROI (circle of 2.5 mm diameter, Figure S3).

2.14. Statistical Analysis. GraphPad Instat (GraphPad Software, San Diego, CA) was used for all statistical measurements; data were reported as mean ± standard deviation. For comparison of data one-way analysis of variance (ANOVA) with a Tukey's post hoc test was used. All differences were considered significant at p-values <0.05.

3. RESULTS AND DISCUSSION

3.1. Simultaneous Labeling of CPC with PFCE-Loaded PLGA and Gold Nanoparticles. To label the cement for ^{19}F MRI, we used PFCE-loaded PLGA nanoparticles. These nanoparticles were developed at the Radboud University Medical Center (Nijmegen, The Netherlands) and are now being prepared for use in clinical trial for labeling dendritic cell-based vaccines (clinicaltrial.gov identifier NCT02574377).[35] These particles typically have a hydrodynamic radius of 100 nm, as determined by DLS, and zeta-potential values in a range of −1 to −5 mV, due to steric stabilization by poly(vinyl alcohol). A scanning electron microscope (SEM) image of the nanoparticles is shown in Figure 1A. The amount of PFCE in
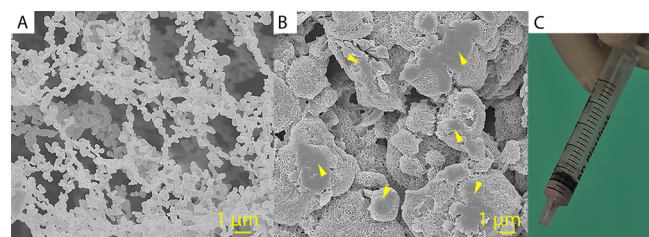

Figure 1. Scanning electron micrographs of the PFCE-loaded PLGA nanoparticles (A) and of the surface of a preset cylinder of CPC/PFCE/gold (B). Yellow arrows indicate the agglomerates of PLGA/PFCE nanoparticles that appeared after the material preparation. Scale bar 1 μm. In (C) a 2 mL syringe containing CPC/PFCE/gold paste is shown.

the particles was determined by nuclear magnetic resonance (NMR) using an internal reference and was around 20 wt %. As CT contrast agent, we used commercially available AuNPs that are stabilized with citric acid in PBS.

The largest initial challenge was the incorporation of both nanoparticle labels into the CPC matrix. Earlier combinations of CPCs and several contrast agents were produced by mixing the dried powders and therefore had only one easy production step.[13−18] However, our PFCE-loaded PLGA nanoparticles formed clusters in the freeze-dried state, making homogeneous incorporation into the CPC difficult. Moreover, AuNPs were provided dispersed in PBS solution. Therefore, we developed an easy two-step method that allowed for the simultaneous incorporation of both nanoparticles into the CPC phase. All

components were independently dispersed in water and mixed at high shear stress followed by fast freezing and freeze-drying the mixture to avoid the setting of CPC. In the second step, the obtained dual labeled-CPC powder could be mixed with the setting solution and handled further as the nonlabeled CPC. This method was more efficient for incorporation of both labels than adding the imaging agents, mixing them in the setting solution, or mixing the cement directly with freeze-dried powder of nanoparticles. The color of the cement composite changed from white to pink after AuNPs were added (Figure 1C). The uniform distribution of color in CPC indicated a homogeneous distribution of AuNPs. Morphological analysis based on SEM (Figure 1B and Figure S4) proved that PFCE-loaded PLGA nanoparticles were incorporated into the CPC matrix. After incorporation and setting of the CPC, the initial PFCE-loaded PLGA nanoparticles formed clusters of approximately 1−5 μm in diameter. This cluster formation could be due to reduced colloidal stability of nanoparticles in the cement mixture and to the relatively high concentration of nanoparticles at 17% w/w.[44] However, MR imaging of labeled CPC revealed that these agglomerates were homogeneously distributed in the cement matrix (Figure 2C). Thus, the agglomeration did not influence the imaging properties of the
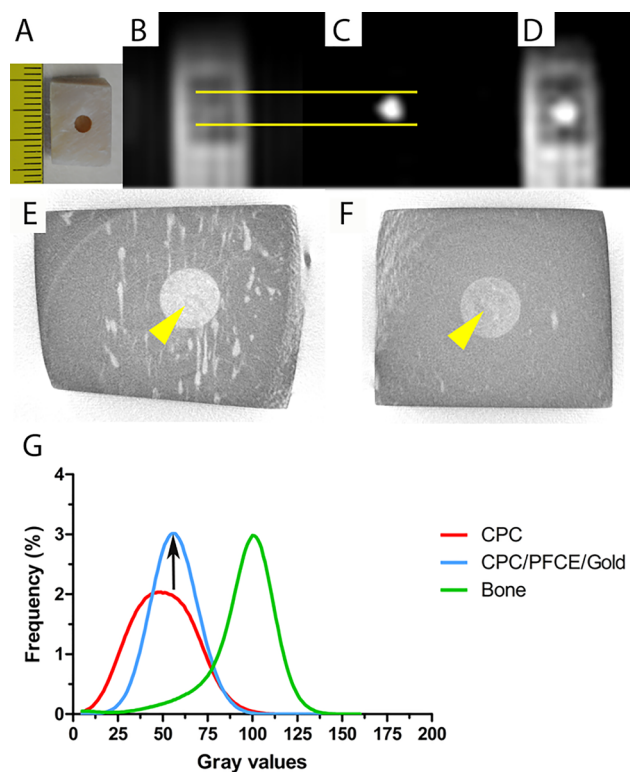
Figure 2. In vitro MRI and CT imaging of a bone block obtained from pig jaw. In (A) the morphological representation of the bone block. In (B) and (C) ^{1}H and ^{19}F ZTE MR images of CPC/PFCE/gold composite obtained at 11.7 T. Note that the ^{19}F signal corresponds to the cylindrical defect in the ^{1}H ZTE image as highlighted by the yellow lines. (D) ZTE MR images of ^{19}F overlaid on those of ^{1}H ZTE. In (E) and (F) the gray scale 2D images from the μCT of the pig block filled with the CPC composite are shown without (E) and with (F) contrast agents. The yellow arrows indicate the implanted material. In (G) the graph from the gray values distribution calculated for a defined volume of interest (n = 3). Note that the signal intensity is elevated and much more defined.
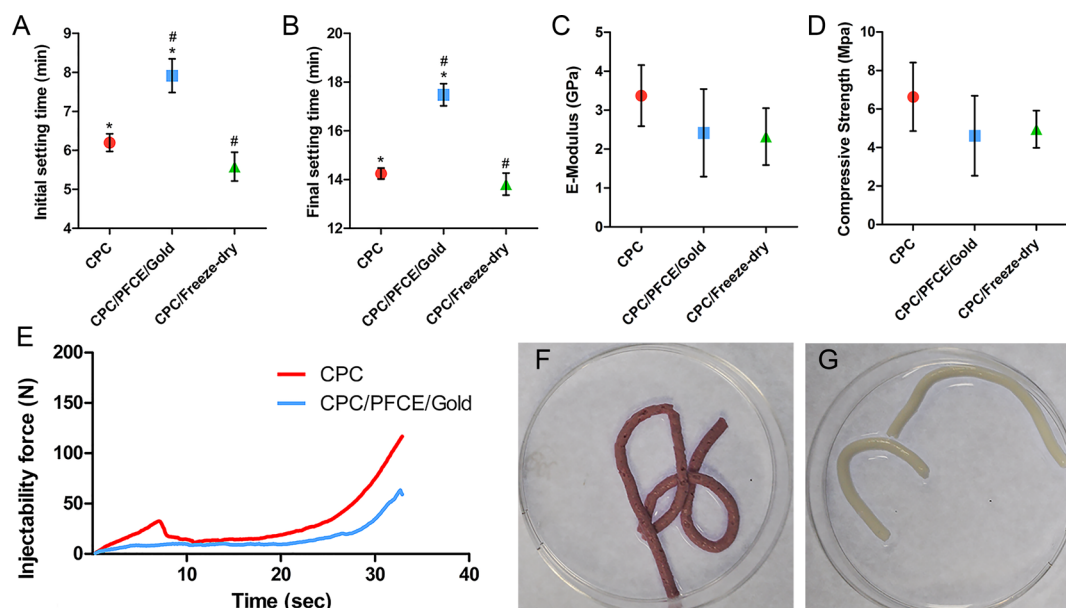
Figure 3. Mechanical and handling properties of the CPC composite with and without contrast agents, respectively; the initial (A) and the final (B) setting time from Gilmore tests ($n = 3$); the E-modulus (C) and the compressive strength (D) from the compression tests ($n = 5$); the extrusion curves from the injectability tests (E) ($n = 3$); CPC/PFCE/gold composite (F) and CPC (G) representative samples from cohesion tests ($n = 3$). # and ∗ mean $p < 0.05$.

final material. Likely, this agglomeration could even be an advantage for our purpose due to possibly slower degradation of aggregated nanoparticles that allowed the PFCE signal to last longer in the CPC matrix. Unfortunately, the AuNPs were too small to be identified by SEM in the morphologically complex CPC matrix. However, the change of the color and the enhanced CT visibility indicated that the incorporation was successful (Figure 2E−G).

3.2. Imaging of Cement Injected in Vitro in Pig Jaw Blocks. To find out the optimal ratio between the CPC powders and the contrast agents, we performed μCT and ^{19}F MR imaging of the final material. On the basis of these results, we determined that a concentration of 20 mg of freeze-dried PFCE-loaded PLGA nanoparticles per 100 mg of CPC powder provided sufficient labeling with PFCE. For CT contrast, 1 mL of AuNPs suspension was necessary for significant enhancement (data not shown).

Next, we imaged CPC composites injected in pig bone blocks (Figure 2A) using ^{1}H and ^{19}F MRI. On the ^{1}H MR image (Figure 2B), CPC could not be distinguished from pig bone. However, a strong fluorine signal was detected from the CPC/PFCE/gold composite in the ^{19}F ZTE MR image (Figure 2C). Thus, overlaying the ^{19}F on the ^{1}H image allowed identification of the labeled CPC (Figure 2D).

Two-dimensional gray scale images of the CPC injected in pig blocks were obtained by μCT acquisition. As shown in Figure 2, CPC with contrast agents (Figure 2F) appeared visually darker than nonlabeled CPC (Figure 2E). A quantitative estimation of the gray value distribution confirmed this observation. CPC/PFCE/gold reported significantly higher pixel frequency compared to the CPC control as well as a rightward shift of the gray values curve (Figure 2G). Furthermore, the narrowing of the peak indicated an even distribution of the particles in the CPC phase.

3.3. Characterization of the Handling and Mechanical Properties. The mechanical and handling properties of the final cement mixture are very important for the application as a bone filler. These mechanical properties should match those of the treated bone. Furthermore, the in situ setting should be fast but also provide enough time for the surgeon to implant and model the paste. Further, hydraulic features should allow easy injection of the material, enabling minimally invasive operations.[4−6] To investigate whether the incorporation of the two types of nanoparticles affected the material properties of the CPC, we performed handling and mechanical testing. As a control we used CPC that was treated in the usual way (CPC-control) and another CPC that we prepared in the same way as the labeled CPC but without nanoparticles (CPC/freeze-dried). The last control is important as possible changes in material properties can be caused either by incorporation of nanoparticles or by the extra steps involving resuspension in water and freeze-drying. Setting times of the CPC/PFCE/gold composite that we obtained from the Gillmore tests (Figure 3A,B) showed an increase in the initial and final times by 1.7 ± 0.3 min and 3.2 ± 0.3 min, respectively, compared to CPC-control. However, this small increase did not affect injection during surgery. Setting times of both nonlabeled CPC controls—the freeze-dried and the non-freeze-dried—were similar to each other. This behavior indicates that the incorporation of the particles did cause an increase in setting time. Ideally, the initial setting time should be between 6 and 10 min, and the final hardening should be reached within 20 min.[5,6] Thus, the setting time of our labeled composite is within this range confirming that it can be used as a bone implant.

Comparing the compressive strength and the E-modulus of the CPC/PFCE/gold composite to the nonlabeled CPC showed that labeling does not affect the mechanical properties of CPC (Figure 3C,D). Particularly, both values are similar compared to the CPC that was only freeze-dried (i.e., CPC/freeze-dried), indicating that the freeze-drying rather than the incorporation of the nanoparticles affected the properties of the final material. Importantly, these differences were not significantly different when compared to standard CPC. Thus, compressive strength and E-modulus are comparable with the

values of the most common α-TCP composites reported in the literature that are typically between 1 and 70 MPa and 0.5 and 9 GPa, respectively, depending on the exact composition of the material.[5] In particular, a commercially available injectable bone cement, chronOST™ Inject, has a compressive strength of 3.0 ± 0.6 MPa.[44] This value is very close to the results of this study (i.e., CPC/PFCE/gold = 4.6 ± 2.1 MPa) meaning that our composite could be used for similar applications. Surely, CPC/PFCE/gold is indicated for nonload-bearing bone defects, specifically in cancellous bone, which shows similar compressive strength and elasticity (i.e., 4–12 MPa and 0.1–0.5 GPa, respectively).[46]

Finally, CPC/PFCE/gold composite showed excellent hydraulic and cohesive features. All samples could be completely extruded from the syringe through a 1.7 mm orifice and thereafter set in an aqueous solution (Figure 3E–G and Figure S5). Even if we used no needles in this study, our results indicate that CPC/PFCE/gold composite is suitable for use with needles up to 15 gauge. Such needles are used, for example, in several back and face surgeries.[6,39]

3.4. Imaging of Cement Injected in Vivo in Rat Bone Model.
Having promising in vitro results on both imaging and materials properties, we then investigated the performance of our labeled composite in vivo for longitudinal monitoring up to 8 weeks from the injection in a rat femoral condyle defect. This defect involves relatively simple surgery and is a well-established nonload-bearing model to study bone biomaterials.[42] The time of 8 weeks was chosen, as we expected from our in vitro study (data not shown) and from previous works on CPC degradation in the same model, that the CPC would stay in the bone for at least 4 weeks.[17,18]

For in vivo testing, we used non freeze-dried CPC as a control as well as another group of animals with an empty defect. None of the animals showed any sign of discomfort, swelling, or restriction in movement after surgery. To monitor the cement after injection, we performed MRI and CT image acquisitions immediately after surgery (i.e., day 0), and at 4 and 8 weeks postsurgery. High-resolution anatomical MR images of the rat leg were acquired at day 0, 4 weeks and 8 weeks after injection (Figure S6). As expected from in vitro imaging results, it was not possible to distinguish the nonlabeled CPC composite in rat legs from the surrounding bone on ¹H ZTE images. In contrast, after injection, the labeled composite could be imaged with both MRI and CT for the whole duration of 8 weeks.

The shape of the labeled composite was clearly recognizable on ¹⁹F ZTE MR images, shown in false color, providing precise geometrical information (Figure 4). Moreover, comparing the images at different time-points after injection showed that the ¹⁹F signal area was shrinking. Indeed, further quantitative analysis of ¹⁹F signal confirmed this observation and showed a gradual decrease of the ¹⁹F-containing region over 8 weeks (Figure 5). Moreover, this reduction in signal area correlates to the decrease in the volume of the implant as a consequence of cement degradation. This suggests that dissolution of the cement causes clearance of the PFCE-loaded PLGA nanoparticles, resulting in a signal decrease.

Because of the high calcium salts content, CPCs generally show higher radiographic attenuation when compared to the natural bone phase.[10] However, there are many available calcium phosphate-based composites which may consist of different mineral components (i.e., α-TCP, hydroxyapatite) often combined with different additives, polymers, or fibers.[4–6]
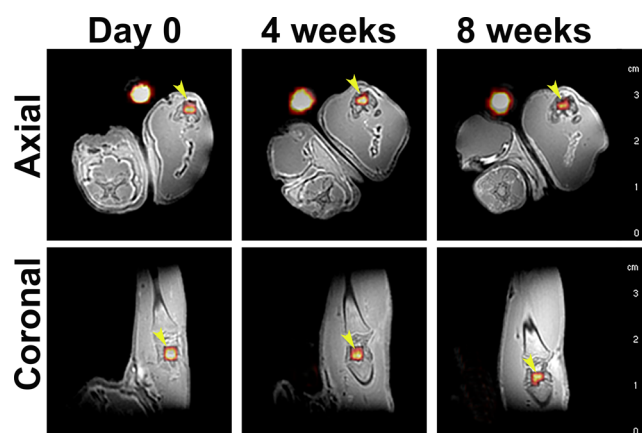
Figure 4. Representative in vivo ZTE MR images of ¹⁹F overlaid on those of ¹H of a rat leg at day 0, 4 weeks and 8 weeks in axial and coronal directions. The presence of ¹⁹F is shown in false color. Yellow arrows indicate the implanted material, while the bright yellowish spot next to each leg corresponds to the reference (i.e., Eppendorf tube containing PFCE-loaded nanoparticles dispersed in water).
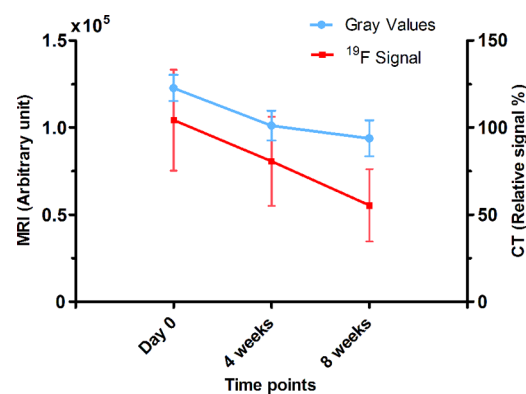

Figure 5. ¹⁹F MRI and CT signal quantification of the CPC/PFCE/gold composite at day 0, 4 weeks and 8 weeks. ¹⁹F signal (red) in ¹⁹F ZTE MR images and relative signal (blue) in CT images were quantified and expressed as arbitrary unit and in percentage of relative attenuation intensity, respectively ($n = 8$). Lines indicate the trend of the data points.

Depending on the specific mixture of components, CPCs may show different X-ray attenuation, with better or worst contrast when compared to the natural bone. Thus, a "natural" contrast between CPC and bone is not always a given yet is dependent on parameters, such as the CPC composition, the type/density of the bone, and the biological phase of bone remodeling. We aimed to achieve a labeling methodology in which, irrespective of these circumstances, a reliable contrast can always be achieved. Composites with improved contrast are demanded especially when need to be injected in the vertebral spine. In such clinical circumstances, leakage of CPC from the vertebral body can occur leading to several symptomatic complications (i.e., neurological complication, collapse of the adjacent vertebrae).[11,12] A clear view of the implanted CPC can be also hindered by the presence of extensive soft tissue around the implant that can obscure its precise shape identification.[11] Furthermore, CPC monitoring over time is changeling and less precise. It has been proven that only after disappearance of the 50% of the implanted material and subsequent replacement with new bone is it possible to recognize a visible change in bone remodeling.[10,11] CPC/PFCE/gold composite showed not

only visual enhancement of CT attenuation right after the surgery (i.e., day 0), but the shape of the implant was clearly visible during the all duration of the experiment (Figure 6). By contrast, the nonlabeled CPC used as control shows similar attenuation as the natural bone phase. Although it is possible to identify the implanted nonlabeled CPC after surgery, the border between the bone and the implanted cement was not always recognizable. The identification of the implanted control cement became more challenging at 4 weeks postsurgery after the CPC degradation took place (Figure 6). Evaluation of the mean attenuation coefficients expressed in Hounsfield unit (HU) per mm^3 confirmed these results. At all the time points, the CPC/PFCE/gold composite showed higher values than both empty defect group and nonlabeled CPC composite (Figure 6). However, this difference was statistically relevant only at 4 and 8 weeks. The higher signal intensity from the CPC/PFCE/gold composite allowed for a better definition of implant shape and volume, in comparison to the nonlabeled CPC. A narrowing of the shape of the labeled implant was clearly visible for all the experimental times. For this reason, CT acquisitions enabled a more precise quantification of the volume of the labeled implant at each time point. Moreover, by comparing the relative signal intensities over time, it was possible to see a gradual decrease of the signal intensity, indicating clearance of the label with cement degradation (Figure 5). Only few studies on the long-term imaging of radiopaque bone substitutes are available. However, most of these studies concern in vitro tests or focus on in vivo biological response without imaging its degradation.[13−16] In a previous study, Ventura et al. used smaller AuNPs with 4 nm diameter that were embedded in silica matrix to enhance CT contrast.[17] However, these nanoparticles diffused from the silica particles 4 weeks after the implantation in vivo, resulting in loss of CT contrast. In this study, larger nanoparticles with diameter of 40 nm provided long-term enhancement CT contrast, at least up to 8 weeks. We assume the bigger size of AuNPs hindered the diffusion of nanoparticles out of CPC, resulting in prolonged enhancement of CT.

Finally, the combination of both imaging modalities enabled to monitor degradation of the cement. To compare quantitative MRI and CT signals, we investigated if there is a correlation between ^{19}F MRI signal, CT attenuation coefficient, and volume of the implant at each time point. The Pearson correlation coefficients and confidence intervals are summarized in Table 1. Pearson coefficients were ranked according to the rule of thumb.[43] Very strong (i.e., $0.9 < r < 1$) and strong (i.e., $0.7 < r < 0.9$) statistically significant linear relationships (i.e., $p < 0.05$) between the two variables were found at day 0 and at 4 weeks, respectively, for correlation of MRI signal to implant volume, CT signal to implant volume, and MRI signal to CT signal. In contrast, at 8 weeks, a strong linear correlation was found between CT signal and volume of the implant, while the relationships between MRI signal and implant volume or MRI signal and CT signal were low and moderate respectively (i.e., moderate = $0.5 < r < 0.7$, low = $0.3 < r < 0.5$). This lower correlation of MRI signal could be due to limited MRI resolution for such a small implant volume (i.e., $<4.41 \pm 1.96$ mm^3), resulting in relatively few voxels over the implant and thus larger error due to the partial volume effect.[29] However, both MRI and CT demonstrated that the degradation of the cement mainly occurred as a gradual process of dissolution that starts from the edges of the implant. Thus, in total, it was
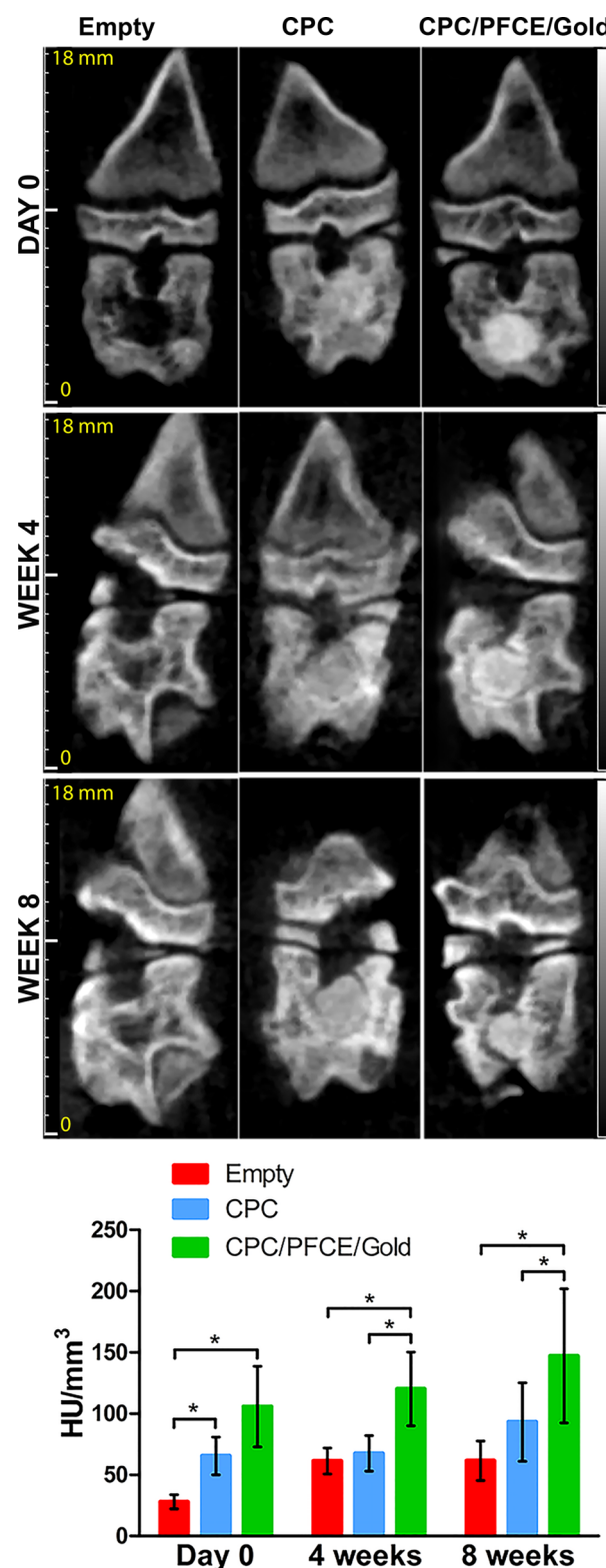
Figure 6. Qualitative and quantitative in vivo CT results. The CT images of the coronal direction of the rat femoral condyle are shown for defects left empty or/and filled with CPC alone or/and with CPC/PFCE/gold. From the top to the bottom, the pictures of the same specimen are shown directly after the surgery (day 0) and at 4 and 8 weeks postsurgery. The bar graph presents the signal quantification estimated by IRW, based on a defined region of interest. Values are reported as mean of attenuation coefficients in HU per the total volume in mm^3 ($n = 8$).

Table 1. Correlation Analysis Comparing Mean Intensities from ^{19}F MRI Signal, CT Attenuation Coefficient, and Implant Volume

		Pearson (ρ)	$p < 0.05$	95% interval of confidence
day 0	CT vs volume	0.88	yes	$0.39 < \rho < 0.96$
	MRI vs volume	0.79	yes	$0.13 < \rho < 0.96$
	CT vs MRI	0.88	yes	$0.43 < \rho < 0.98$
4 weeks	CT vs volume	0.93	yes	$0.62 < \rho < 0.99$
	MRI vs volume	0.95	yes	$0.70 < \rho < 0.96$
	CT vs MRI	0.79	yes	$-0.01 < \rho < 0.95$
8 weeks	CT vs volume	0.82	yes	$0.22 < \rho < 0.97$
	MRI vs volume	0.41	no	$0.46 < \rho < 0.88$
	CT vs MRI	0.56	no	$-0.29 < \rho < 0.92$

possible to follow CPC degradation qualitatively and quantitatively up to 8 weeks postsurgery.

The versatility of a dual-labeling approach allows to produce patient-tuned composites that could include either both or only one of the two contrast agents depending on the specific bone applications. In imaging-guided vertebroplasty a CPC composite with initial enhanced CT contrast is preferred by the surgeons as it can help for the identification of any cement leakage.[11] By contrast, when the monitoring of the material degradation over time and the subsequent bone regeneration become the crucial aspect, e.g., in orthopedic and maxillofacial applications, a noninvasive imaging modality (i.e., MRI) is alternatively suggested.[6]

Multimodal imaging approaches (i.e., PET/CT, PET/MRI) have gained clinical interest over the past years as two imaging modalities can provide synergistic benefits.[23] In this study a multimodal visible bone substitute (i.e., visible by either CT or MRI) was developed. Such dual-labeled composite could give to the radiologists the possibility to provide a patient-tailored imaging workflow according to each specific clinical circumstance (i.e., CT acquisition could be performed right after the surgery, while MRI is applied for longitudinal monitoring). To date, a CT/MRI multimodal approach is aimed only in preclinical or clinical studies related to bone remodeling and biomaterials development. However, as MRI is superior to CT for many aspects (i.e., it is radiation-free, provides soft and hard tissues contrast, it gives 3D anatomical and functional information) an ultimate long-term focus for research should still be to make MRI as a preferential bone imaging screening tool.[8,22]

Of course, it can also be critically regarded what is the final patient benefit of this labeling procedure. Adding a label to an existing or newly developed medical device will make the device more complex to understand and control in its biological behavior, more difficult and timely to pass through legislation procedures, and moreover it will inevitably make the treatment itself more costly. Thus, it could be foreseen that the major importance of labeling procedures in general is in the phases of preclinical and clinical research, and it is not always necessary to incorporate labels into the finally developed medical device for clinical use. The use of labeling might be very dependent on the field of application. For instance, in dental treatment patients who receive a bone filler in a periodontal lesion will be repetitively subjected to imaging during regular follow-up anyways; whereas for other types of surgery the follow-up period stops after initial healing. Imaging agents would there only be necessary if special indications necessitate a more long-

term follow-up, for instance in oncologic patients, or patients that are monitored regularly due to systemic disease (e.g., severe osteoporosis or diabetes). Even then, incorporation of a contrast is only necessary when the diagnostic imaging sessions for the patient can also result in consequences for the treatment, like early detection and planning of revision surgery.

3.5. Bone-Growth Assessment by Histology and Histomorphometry. To investigate the tissue reaction on the CPC composites with and without imaging nanoparticles, we made histological sections at week 8. Because of the decalcification process during histological preparation, it was not possible to detect CPC remnants in the sections. However, the circular area of the original defect was still clearly recognizable, and thus we used this area for qualitative and quantitative analysis (Figure 7). The empty defect group shows
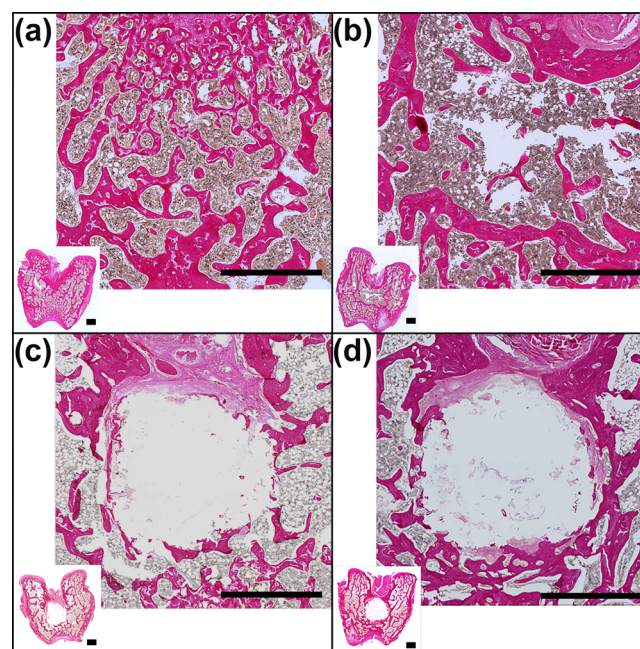

Figure 7. Histological sections of the femora stained with EVG after 8 weeks of implantation. The original bone structure in (A), the empty defect in (B), the defect filled with CPC in (C), and the defect filled with CPC/PFCE/gold composite in (D) are shown. For each specimen, a picture of the general overview taken at 1× magnification (inset) and the respective zoomed view (magnification 10×) are shown. The markers correspond to 1 mm.

incomplete healing proving that the performed defect was a critical-size defect for the 8 week period. Furthermore, both labeled and nonlabeled CPC materials did not induce any immune response or fibrotic encapsulation. However, in several samples, a layer of fibrous tissue was present at the interface between bone and implant. This layer was not always continuous and appeared to contain fibrous tissue and immature extracellular matrix fibers, yet often also showed red-stained calcified nodules, indicating the onset of mineralization. This effect was present in 1/8 samples of the CPC group and 4/8 samples of the CPC/PFCE/gold group. χ^2 testing demonstrated that such frequencies are not significantly different ($p > 0.05$) between both groups. In all cases, there was direct contact between bone and CPC, and uniform bone growth in all the groups was observed. Such bone growth began at the edges and then proceeded throughout the entire contact area toward the inside of the implant.

Histomorphometrical analysis of a defined ROI (i.e., circle of 2.5 mm in diameter) demonstrated the relative formation of the new bone, with approximate filling of defect of 50%, which is typical for this length of time.[17] No statistical differences in bone content were found between the empty defect group, the CPC group, and the CPC/PFCE/gold group (Figure 8). This
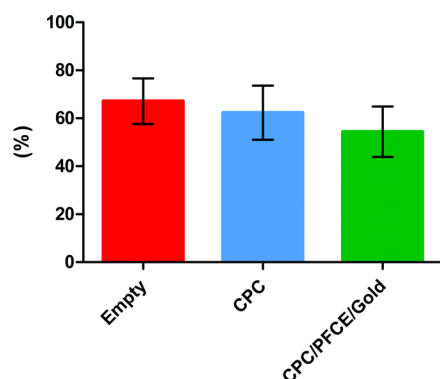
Figure 8. Relative bone formation quantification based on histology performed after 8 weeks from the surgery ($n = 8$). No statistical differences were found.

new bone formation is in the range of the decrease of both MRI and CT signals. Aiming at clinical application, further studies with longer experimental times and with materials of differing degradation kinetics could help to develop a reliable method for quantitative monitoring the degradation with MRI and CT contrasts in vivo.

One limitation of the presented experimental model was that we did not focus on the clearance of the applied labels from the body. However, many previous investigations studied body uptake of either perfluorocarbons (PFCs) or gold nanoparticles (AuNPs) as well as their biological compatibility.[34,36,47−50] Specifically, it has been proven that PFCs are first removed from the blood circulation by reticuloendothelial system filtration and also can ultimately be exhaled through the respiration system.[34,36] Differently, AuNPs uptake seems to be size-dependent. Small AuNPs (i.e., 5−15 nm) are excreted through kidney filtration, while large particles (>200 nm) are captured by the immune system and delivered into the liver or the spleen.[47,48] After 24 h from intravenous administration of 50 nm AuNPs in a rat model, particles showed accumulation only in the blood, liver, and spleen.[49] Therefore, it could be speculated that the 40 nm AuNPs used in this study would undergo a similar fate and finally be eliminated from the body through the feces.[50] Another consideration is the concentration of contrast agents used for the preparation of the CPC/PFCE/gold composite. Specifically, the estimated PFCE concentration is less than 5 mg per 100 mg of cement. Such concentration is considerably low when compared to the large concentration that is requested when PFCs are used in the blood circulation (i.e., about 10 g/kg).[36] Similarly, the used gold concentration (i.e., about 0.5 mg per 100 mg of cement) resulted to fall in the "therapeutic window" within which AuNPs can be used without any side effects, suggesting that an even higher concentration may be investigated for further improvement of the CT contrast.[48]

4. CONCLUSIONS

Nowadays, one of the main challenges in tissue engineering is to develop detectable materials that can be followed longitudinally once implanted in the body. Here, we propose an innovative ceramic material with enhanced ^{19}F MRI and CT contrast for bone application. By labeling a CPC with PLGA/PFCE and AuNPs, we obtained a composite that can be qualitatively and quantitatively detected until 8 weeks postsurgery in an in vivo rat model of bone regeneration. Thus, our CPC/PFCE/gold provided more correct anatomical and functional information, with both MRI and CT, helping to overcome the imaging limitation of ceramics materials. Successful development of this CPC composite has substantial potential for clinical use.

The combination of the current contrast agents-based strategy is suggested for all kinds of ceramic materials as well as for polymeric scaffold or hydrogels. Certainly, for every different material or application, a certain degree of customization (e.g., fine-tuning the amount of nanoparticles) is required. For ceramics, PFCE could be incorporated in specific cement-dedicated carriers (e.g., microrods, fibers, bigger particles). Simultaneously, gold could be directly combined with the carrier containing PFCE by following many strategies, such as coating or incorporation in bigger beads. In this way, specific-cement-dedicated carriers can easily be developed and scaled-up for clinical applications. Furthermore, further improvement of the biological properties of the dual-labeled CPC composite could be pursuit by adding specific growth factors (i.e., BMP-2) which can be used to trigger new bone formation.

■ ASSOCIATED CONTENT

ⓢ Supporting Information

The Supporting Information is available free of charge on the ACS Publications website at DOI: 10.1021/acsami.7b04075.

Surgical procedure, CT signal quantification, bone quantification based on histology, SEM of CPC/PFCE/gold, cohesion test, ^{1}H MR image of rat bone (PDF)

■ AUTHOR INFORMATION

Corresponding Author

*(X.F.W.) E-mail: frank.walboomers@radboudumc.nl.

ORCID ⓘ

X. Frank Walboomers: 0000-0001-5742-9826

Author Contributions

S.M. and W.D. contributed equally to this work. A.H. and M.S. contributed equally to this work.

Notes

The authors declare no competing financial interest.

■ ACKNOWLEDGMENTS

Lemmers-van der Weem, Eric van Dinther, Edyta Swider, and Andor Veltien BSc.

■ ABBREVIATIONS

CPC, calcium phosphate cement; PFCE, perfluoro-15-crown-5-ether; AuNPs, gold nanoparticles.

■ REFERENCES

(1) Campana, V.; Milano, G.; Pagano, E.; Barba, M.; Cicione, C.; Salonna, G.; Lattanzi, W.; Logroscino, G. Bone Substitutes in Orthopaedic Surgery: from Basic Science to Clinical Practice. *J. Mater. Sci.: Mater. Med.* **2014**, *25*, 2445−61.

(2) Giannoudis, P. V.; Dinopoulos, H.; Tsiridis, E. Bone Substitutes: an Update. *Injury* **2005**, *36* (3), S20−S27.

(3) Albee, F. H. Studies in Bone Growth: Triple Calcium Phosphate as a Stimulus to Osteogenesis. *Ann. Surg.* **1920**, *71*, 32−39.

(4) Habraken, W.; Habibovic, P.; Epple, M.; Bohner, M. Calcium Phosphates in Biomedical Applications: Materials for the Future? *Mater. Today* **2016**, *19*, 69−87.

(5) Zhang, J.; Liu, W.; Schnitzler, V.; Tancret, F.; Bouler, J. M. Calcium Phosphate Cements for Bone Substitution: Chemistry, Handling and Mechanical Properties. *Acta Biomater.* **2014**, *10*, 1035−49.

(6) Low, K. L.; Tan, S. H.; Zein, S. H.; Roether, J. A.; Mourino, V.; Boccaccini, A. R. Calcium Phosphate-based Composites as Injectable Bone Substitute Materials. *J. Biomed. Mater. Res., Part B* **2010**, *94*, 273−86.

(7) Beaman, F. D.; Bancroft, L. W.; Peterson, J. J.; Kransdorf, M. J.; Menke, D. M.; DeOrio, J. K. Imaging Characteristics of Bone Graft Materials. *Radiographics* **2006**, *26*, 373−88.

(8) Ventura, M.; Boerman, O. C.; de Korte, C.; Rijpkema, M.; Heerschap, A.; Oosterwijk, E.; Jansen, J. A.; Walboomers, X. F. Preclinical Imaging in Bone Tissue Engineering. *Tissue Eng., Part B* **2014**, *20*, 578−95.

(9) Brenner, A. I.; Koshy, J.; Morey, J.; Lin, C.; DiPoce, J. The Bone Scan. *Semin. Nucl. Med.* **2012**, *42*, 11−26.

(10) Larsson, S. Calcium Phosphates: What is the Evidence? *J. Orthop. Trauma* **2010**, *24* (1), S41−S45.

(11) Acarturk, O.; Lehmicke, M.; Aberman, H.; Toms, D.; Hollinger, J. O.; Fulmer, M. Bone Healing Response to an Injectable Calcium Phosphate Cement with Enhanced Radiopacity. *J. Biomed. Mater. Res., Part B* **2008**, *86B*, 56−62.

(12) Wang, X.; Ye, J.; Wang, Y. Influence of a Novel Radiopacifier on the Properties of an Injectable Calcium Phosphate Cement. *Acta Biomater.* **2007**, *3*, 757−63.

(13) Hoekstra, J. W.; van den Beucken, J. J.; Leeuwenburgh, S. C.; Bronkhorst, E. M.; Meijer, G. J.; Jansen, J. A. Tantalum Oxide and Barium Sulfate as Radiopacifiers in Injectable Calcium Phosphate-Poly(Lactic-co-Glycolic Acid) Cements for Monitoring In Vivo Degradation. *J. Biomed. Mater. Res., Part A* **2014**, *102*, 141−9.

(14) Pepiol, A.; Teixidor, F.; Saralidze, K.; van der Marel, C.; Willems, P.; Voss, L.; Knetsch, M. L.; Vinas, C.; Koole, L. H. A Highly Radiopaque Vertebroplasty Cement Using Tetraiodinated O-Carborane Additive. *Biomaterials* **2011**, *32*, 6389−98.

(15) Wang, J. S.; Diaz, J.; Sabokbar, A.; Athanasou, N.; Kjellson, F.; Tanner, K. E.; McCarthy, I. D.; Lidgren, L. In Vitro and In Vivo Biological Responses to a Novel Radiopacifying Agent for Bone Cement. *J. R. Soc., Interface* **2005**, *2*, 71−8.

(16) Boelen, E. J.; Lewis, G.; Xu, J.; Slots, T.; Koole, L. H.; van Hooy-Corstjens, C. S. Evaluation of a Highly-Radiopaque Iodine-Containing Acrylic Bone Cement for Use in Augmentation of Vertebral Compression Fractures. *J. Biomed. Mater. Res., Part A* **2008**, *86*, 76−88.

(17) Ventura, M.; Sun, Y.; Rusu, V.; Laverman, P.; Borm, P.; Heerschap, A.; Oosterwijk, E.; Boerman, O. C.; Jansen, J. A.; Walboomers, X. F. Dual Contrast Agent for Computed Tomography and Magnetic Resonance Hard Tissue Imaging. *Tissue Eng., Part C* **2013**, *19*, 405−16.

(18) Ventura, M.; Sun, Y.; Cremers, S.; Borm, P.; Birgani, Z. T.; Habibovic, P.; Heerschap, A.; van der Kraan, P. M.; Jansen, J. A.; Walboomers, X. F. A Theranostic Agent to Enhance Osteogenic and Magnetic Resonance Imaging Properties of Calcium Phosphate Cements. *Biomaterials* **2014**, *35*, 2227−33.

(19) Lusic, H.; Grinstaff, M. W. X-ray-Computed Tomography Contrast Agents. *Chem. Rev.* **2013**, *113*, 1641−66.

(20) Lee, N.; Choi, S. H.; Hyeon, T. Nano-Sized CT Contrast Agents. *Adv. Mater.* **2013**, *25*, 2641−60.

(21) Xu, C.; Tung, G. A.; Sun, S. Size and Concentration Effect of Gold Nanoparticles on X-ray Attenuation As Measured on Computed Tomography. *Chem. Mater.* **2008**, *20*, 4167−4169.

(22) Griffith, J. F.; Genant, H. K. New Imaging Modalities in Bone. *Curr. Rheumatol. Rep.* **2011**, *13*, 241−50.

(23) Lan, S. M.; Wu, Y. N.; Wu, P. C.; Sun, C. K.; Shieh, D. B.; Lin, R. M. Advances in Noninvasive Functional Imaging of Bone. *Acad. Radiol.* **2014**, *21*, 281−301.

(24) Sun, Y.; Ventura, M.; Oosterwijk, E.; Jansen, J. A.; Walboomers, X. F.; Heerschap, A. Zero Echo Time Magnetic Resonance Imaging of Contrast-Agent-Enhanced Calcium Phosphate Bone Defect Fillers. *Tissue Eng., Part C* **2013**, *19*, 281−7.

(25) Liu, T.; Spincemaille, P.; de Rochefort, L.; Wong, R.; Prince, M.; Wang, Y. Unambiguous Identification of Superparamagnetic Iron Oxide Particles Through Quantitative Susceptibility Mapping of the Nonlinear Response to Magnetic Fields. *Magn. Reson. Imaging* **2010**, *28*, 1383−9.

(26) Wang, Y. X.; Hussain, S. M.; Krestin, G. P. Superparamagnetic Iron Oxide Contrast Agents: Physicochemical Characteristics and Applications in MR Imaging. *Eur. J. Radiol.* **2001**, *11*, 2319−31.

(27) Ebifegha, M. E.; Code, R. F.; Harrison, J. E.; McNeill, K. G.; Szyjkowski, M. In Vivo Analysis of Bone Fluoride Content via NMR. *Phys. Med. Biol.* **1987**, *32*, 439−51.

(28) Code, R. F.; Harrison, J. E.; McNeill, K. G. In Vivo Measurement of Accumulated Bone Fluorides by Nuclear Magnetic Resonance. *J. Bone Miner. Res.* **1990**, *5* (1), S91−S94.

(29) Srinivas, M.; Heerschap, A.; Ahrens, E. T.; Figdor, C. G.; de Vries, I. J. (19)F MRI for Quantitative In Vivo Cell Tracking. *Trends Biotechnol.* **2010**, *28*, 363−370.

(30) Chen, J.; Lanza, G. M.; Wickline, S. A. Quantitative Magnetic Resonance Fluorine Imaging: Today and Tomorrow. *Wiley Interdiscip. Rev.: Nanomed. Nanobiotechnol.* **2010**, *2*, 431−40.

(31) Tirotta, I.; Dichiarante, V.; Pigliacelli, C.; Cavallo, G.; Terraneo, G.; Bombelli, F. B.; Metrangolo, P.; Resnati, G. (19)F Magnetic Resonance Imaging (MRI): From Design of Materials to Clinical Applications. *Chem. Rev.* **2015**, *115*, 1106−29.

(32) Heerschap, A. In Vivo 19F Magnetic Resonance Spectroscopy. *eMagRes.* **2016**, 1283−1290.

(33) Pisani, E.; Tsapis, N.; Galaz, B.; Santin, M.; Berti, R.; Taulier, N.; Kurtisovski, E.; Lucidarme, O.; Ourevitch, M.; Doan, B. T.; Beloeil, J. C.; Gillet, B.; Urbach, W.; Bridal, S. L.; Fattal, E. Perfluorooctyl Bromide Polymeric Capsules as Dual Contrast Agents for Ultrasonography and Magnetic Resonance Imaging. *Adv. Funct. Mater.* **2008**, *18*, 2963−2971.

(34) Chen, J.; Pan, H.; Lanza, G. M.; Wickline, S. A. Perfluorocarbon Nanoparticles for Physiological and Molecular Imaging and Therapy. *Adv. Chronic. Kidney Dis.* **2013**, *20*, 466−78.

(35) Srinivas, M.; Cruz, L. J.; Bonetto, F.; Heerschap, A.; Figdor, C. G.; de Vries, I. J. Customizable, Multi-Functional Fluorocarbon Nanoparticles for Quantitative In Vivo Imaging Using 19F MRI and Optical Imaging. *Biomaterials* **2010**, *31*, 7070−7.

(36) Ahrens, E. T.; Helfer, B. M.; O'Hanlon, C. F.; Schirda, C. Clinical Cell Therapy Imaging Using a Perfluorocarbon Tracer and Fluorine-19 MRI. *Magn. Reson. Med.* **2014**, *72*, 1696−1701.

(37) Yi, C.; Liu, D.; Fong, C. C.; Zhang, J.; Yang, M. Gold Nanoparticles Promote Osteogenic Differentiation of Mesenchymal Stem Cells Through p38 MAPK Pathway. *ACS Nano* **2010**, *4*, 6439−48.

(38) Heo, D. N.; Ko, W.-K.; Bae, M. S.; Lee, J. B.; Lee, D.-W.; Byun, W.; Lee, C. H.; Kim, E.-C.; Jung, B.-Y.; Kwon, I. K. Enhanced Bone

Regeneration with a Gold Nanoparticle-Hydrogel Complex. *J. Mater. Chem. B* **2014**, *2*, 1584−1593.

(39) Bohner, M.; Baroud, G. Injectability of Calcium Phosphate Pastes. *Biomaterials* **2005**, *26*, 1553−63.

(40) Rorden, C.; Brett, M. Stereotaxic Display of Brain Lesions. *Behav. Neurol.* **2000**, *12*, 191−200.

(41) Srinivas, M.; Boehm-Sturm, P.; Aswendt, M.; Pracht, E. D.; Figdor, C. G.; de Vries, I. J.; Hoehn, M. In Vivo 19F MRI for Cell Tracking. *J. Visualized Exp.* **2013**, *81*, e50802.

(42) van Houdt, C. I.; Preethanath, R. S.; van Oirschot, B. A.; Zwarts, P. H.; Ulrich, D. J.; Anil, S.; Jansen, J. A.; van den Beucken, J. J. Toward Accelerated Bone Regeneration by Altering Poly(D,L-Lactic-co-Glycolic) Acid Porogen Content in Calcium Phosphate Cement. *J. Biomed. Mater. Res., Part A* **2016**, *104*, 483−92.

(43) Mukaka, M. M. Statistics Corner: A Guide to Appropriate Use of Correlation Coefficient in Medical Research. *Malawi Med. J.* **2012**, *24*, 69−71.

(44) Nel, A. E.; Madler, L.; Velegol, D.; Xia, T.; Hoek, E. M.; Somasundaran, P.; Klaessig, F.; Castranova, V.; Thompson, M. Understanding Biophysicochemical Interactions at the Nano-Bio Interface. *Nat. Mater.* **2009**, *8*, 543−57.

(45) Luo, J.; Ajaxon, I.; Ginebra, M. P.; Engqvist, H.; Persson, C. Compressive, Diametral Tensile and Biaxial Flexural Strength of Cutting-Edge Calcium Phosphate Cements. *J. Mech. Behav. Biomed. Mater.* **2016**, *60*, 617−27.

(46) Wagoner Johnson, A. J.; Herschler, B. A. A Review of the Mechanical Behavior of CaP and CaP/Polymer Composites for Applications in Bone Replacement and Repair. *Acta Biomater.* **2011**, *7*, 16−30.

(47) Rivera-Gil, P.; Jimenez de Aberasturi, D.; Wulf, V.; Pelaz, B.; del Pino, P.; Zhao, Y.; de la Fuente, J. M.; Ruiz de Larramendi, I.; Rojo, T.; Liang, X. J.; Parak, W. J. The Challenge to Relate the Physicochemical Properties of Colloidal Nanoparticles to their Cytotoxicity. *Acc. Chem. Res.* **2013**, *46*, 743−9.

(48) Fratoddi, I.; Venditti, I.; Cametti, C.; Russo, M. V. How Toxic are Gold Nanoparticles? The State-of-the-Art. *Nano Res.* **2015**, *8*, 1771−1799.

(49) De Jong, W. H.; Hagens, W. I.; Krystek, P.; Burger, M. C.; Sips, A. J.; Geertsma, R. E. Particle Size-Dependent Organ Distribution of Gold Nanoparticles after Intravenous Administration. *Biomaterials* **2008**, *29*, 1912−9.

(50) Paciotti, G. F.; Myer, L.; Weinreich, D.; Goia, D.; Pavel, N.; McLaughlin, R. E.; Tamarkin, L. Colloidal Gold: a Novel Nanoparticle Vector for Tumor Directed Drug Delivery. *Drug Delivery* **2004**, *11*, 169−83.